Chapter-4

Enhanced Functionalities of Isovalently Substituted 0.67($Bi_{1-x}La_xFe_{0.97}Ga_{0.03}O_3$)-0.33($BaTiO_3$) Relaxor Piezoceramics Synthesized via Air Quenching

CHAPTER 4

Enhanced Functionalities of Isovalently Substituted $0.67(Bi_{1-x}La_xFe_{0.97}Ga_{0.03}O_3)$-$0.33(BaTiO_3)$ Relaxor Piezoceramics Synthesized via Air Quenching

4.1 Introduction

As previously discussed in chapter 1, utilizing site engineering techniques, such as rare-earth ion doping, has proven to be an effective strategy for improving the dielectric and ferroelectric properties of perovskite systems. Doping at both the A-site and B-site of $BiFeO_3$ has been found to be advantageous in improving the overall functional properties of the system [73]. Previous studies have demonstrated that the introduction of $BiGaO_3$ can enhance the thermal stability and piezoelectricity of BF-BT compositions without compromising the Curie temperature [102], [216]. The addition of Ga^{3+} to a binary $0.67BiFeO_3$-$0.33BaTiO_3$ composition typically results in the formation of a morphotropic phase boundary (MPB), leading to improved insulation and electromechanical properties [59], [102], [216], [217], [218]. Although the positive effects of rare-earth ion doping on the properties of the BF-BT system have been reported, a systematic study focusing on the effects of lanthanum (La) doping in the BF-BT system remains largely unexplored, with ongoing research in this area. Different rare-earth ions have been found to exert distinct effects on the material's properties. For instance, yttrium doping has been shown to improve the piezoelectric and ferroelectric properties by enhancing the relative density and optimizing the average grain size of the BF-BT system [219]. Holmium substitution in BF-BT has been found to enhance piezoelectric and insulation properties [220]. Lanthanum substitution at the A site in perovskites can have a number of effects on the material's properties. It can affect the band gap, electronic structure, conductivity, ferroelectric and magnetic properties of the material, leading to

changes in its overall properties influencing its use in applications such as solar cells or sensors [188]. Lanthanum substitution has been shown to enhance ferroelectric properties, increase the dielectric constant and Curie temperature, and reduce thermal stability in certain cases [74], [185], [221], [222]. This enhancement can be attributed to the fact that lanthanum substitution reduces lattice distortion in the $BiFeO_3$ system, resulting in a decrease in the Bi-O-Fe bond angle. Consequently, rhombohedral crystals may transform into tetragonal or even cubic structures. Lanthanum substitution also has the potential to affect the ionic and electronic conductivity of the material, thus influencing its suitability for applications such as solar cells or batteries. For example, La substitution has been observed to reduce the magnetic ordering temperature of $BiFeO_3$ and modify the type of magnetic ordering. Furthermore, it may alter the ion coordination within the lattice, thereby impacting characteristics such as ferroelectricity and dielectric properties by inducing changes in the crystal structure. Samarium doping has been found to improve the dielectric properties of the BF-BT system [223].

In this particular chapter, we focus on substituting both the A and B sites of the perovskite structure with La and Ga, respectively. The $0.67(Bi_{1-x}La_xFe_{0.97}Ga_{0.03}O_3)$-$0.33(BaTiO_3)$ solid solution was synthesized using air quenching sintering, because achieving pure perovskite phase formation using conventional solid-state routes proved challenging. Our systematic study aims to identify potential candidate materials to replace lead-based ceramics in high-temperature piezoelectric applications in demanding environments. Specifically, we investigate the effects of lanthanum substitution on the chemical state, crystal structure, microstructure, dielectric properties, and ferroelectric properties, with a focus on establishing correlations among these characteristics. This study provides valuable insights into the effects of lanthanum substitution on the properties of perovskite-based materials, enhancing our understanding of their potential

applications. It is important to note that while the BF-BT system holds promise, ongoing research and further improvements are required to fully explore and exploit its characteristics under specific conditions and applications.

4.2 Experimental Details and Characterization

The $0.67(Bi_{1-x}La_xFe_{0.97}Ga_{0.03}O_3)$-$0.33(BaTiO_3)$ where x=0.01(La1), x=0.03(La3), x=0.05(La5), and x=0.07(La7) solid solution compositions were prepared by traditional solid state route employing air quenching after sintering. High purity AR grade reagents namely Bi_2O_3, La_2O_3, Fe_2O_3, Ga_2O_3, $BaCO_3$ and TiO_2 with purity >99% were used as starting precursors. To compensate for Bi volatility, a 5mol% excess of Bi_2O_3 was added. The stoichiometric amounts of the raw materials were weighed and placed in zirconia jars along with zirconia balls for high-energy planetary ball milling (Retsch-PM 400 GmbH, Germany) at 300 rpm for 24 hours. The obtained suspension was then dried at 120 ^{o}C and then hand grinded to get desirable homogeneity before calcination. The powder was calcined at 850°C for two hours. Following this, it was mixed with 2% water solution of polyvinyl alcohol (PVA), serving as a binding agent, to produce green pellets. Disk-shaped pellets measuring 10 mm in diameter were fabricated by pressing calcined powder using a uniaxial hydraulic press, employing an optimized load of 100 MPa. Subsequently, the pellets were subjected to heat treatment up to 500 °C for a duration of 12 hours to eliminate the binder. Thereafter green pellets were sintered at 980 ^{0}C for 2 hours followed by air quenching to room temperature. The density of the pellets was measured using Archimedes method. The sintered specimens were polished to obtain smooth and shiny parallel surfaces using emery paper with different grit sizes. Electroding of the sintered pellets was performed by applying silver paste, which was subsequently fired at 500°C. DC poling was conducted by subjecting the electroded pellets, immersed in silicone oil,

to a field strength of approximately 4 kV/mm for a duration of 30 minutes. To investigate the crystal structure, morphology, and various properties of the ceramics, several characterization techniques were employed. The crystal structure analysis was conducted using a Rigaku Miniflex 600 benchtop diffractometer (Japan) at a scan rate of 1°/min. Cu Kα radiation with a wavelength of 1.540593 Å and a 2θ step size of 0.02° were utilized. Further confirmation of the formation of the perovskite phase was conducted through Fourier-transform infrared spectroscopy (FTIR) using a Thermo Fisher Scientific instrument (USA). The measurements were carried out at room temperature in KBr mode, with a resolution set at 4 cm^{-1}. Morphological and microstructural analysis of the gold-sputtered sintered pellets of the prepared piezoceramics was carried out using a benchtop scanning electron microscope (ZEISS). The temperature-dependent dielectric permittivity (ε_r) and dissipation factor (tan δ) were measured over the frequency range of 20 Hz to 10 MHz using an impedance analyzer (Keysight E4990A) coupled with a programmable oven system, controlled with software. The measurements were performed at a heating rate of 3 °C per minute, covering a temperature range from 30 °C to 500 °C. The ferroelectric (P-E) hysteresis loops, current response, leakage current, and resistivity were assessed at a frequency of 10 Hz utilizing the Precision Premier LC II instrument from Radiant Technologies, USA. Chemical state characterization of the Fe and O elements was conducted using X-ray photoelectron spectroscopy (XPS) with a Thermo Scientific K-Alpha instrument.

4.3 Results and Discussion

4.3.1 Structural Studies

4.3.1.1 Crystal Structure Analysis

The progressive evolution of room temperature X-ray diffraction (XRD) patterns for the calcined and sintered samples of $0.67(Bi_{1-x}La_xFe_{0.97}Ga_{0.03}O_3)$-$0.33(BaTiO_3)$ where x= 0.01, 0.03, 0.05 and 0.07 are illustrated in Figure 4.1. The XRD patterns of the calcined samples exhibit slight peaks corresponding to reactant impurities at approximately $2\theta \sim 31^{o}$ as depicted in inset of Figure 4.1(a). These impurity peaks are eliminated after sintering at 980 ℃ for 2 hours as confirmed in Figure 4.1(b). To conduct a thorough analysis of the crystal structure, the sintered specimens were ground into a fine powder and subsequently annealed at 550 ℃ for 12 hours to alleviate any unnecessary strain generated during the crushing of the pellets. The XRD patterns of the synthesized compositions reveal the emergence of a pristine perovskite phase, devoid of any discernible trace of reactant impurities. This observation underscores the effective diffusion of $BaTiO_3$ and $BiGaO_3$ into the $BiFeO_3$ lattice, culminating in the development of a binary solid solution. This observation signifies the diffusion of La^{3+} at the A-site and Ga^{3+} at the B-site within the main lattice of the BF-BT system, leading to the formation of a stable solid solution. The absence of peak splitting in the pseudo-cubic (111) and (200) peaks indicate the prevalence of a pseudo-cubic phase, which is consistent with previous findings [188]. At higher angles, broad peak splitting seen in the XRD peaks is due to $K\alpha_2$ contribution. For detailed crystal structure analysis, Rietveld structure refinement was performed with cubic $Pm\bar{3}m$ space group using the "Fullprof Suite." The Rietveld refined XRD pattern fits for all the compositions are depicted in Figure 4.2, providing further confirmation into the crystal structure of the studied materials. The refined crystallographic parameters, along with the reliability factors, and the compositional dependencies of lattice parameters for the $0.67(Bi_{1-x}La_xFe_{0.97}Ga_{0.03}O_3)$-$0.33(BaTiO_3)$ solid solution, are presented in Table 4.1.

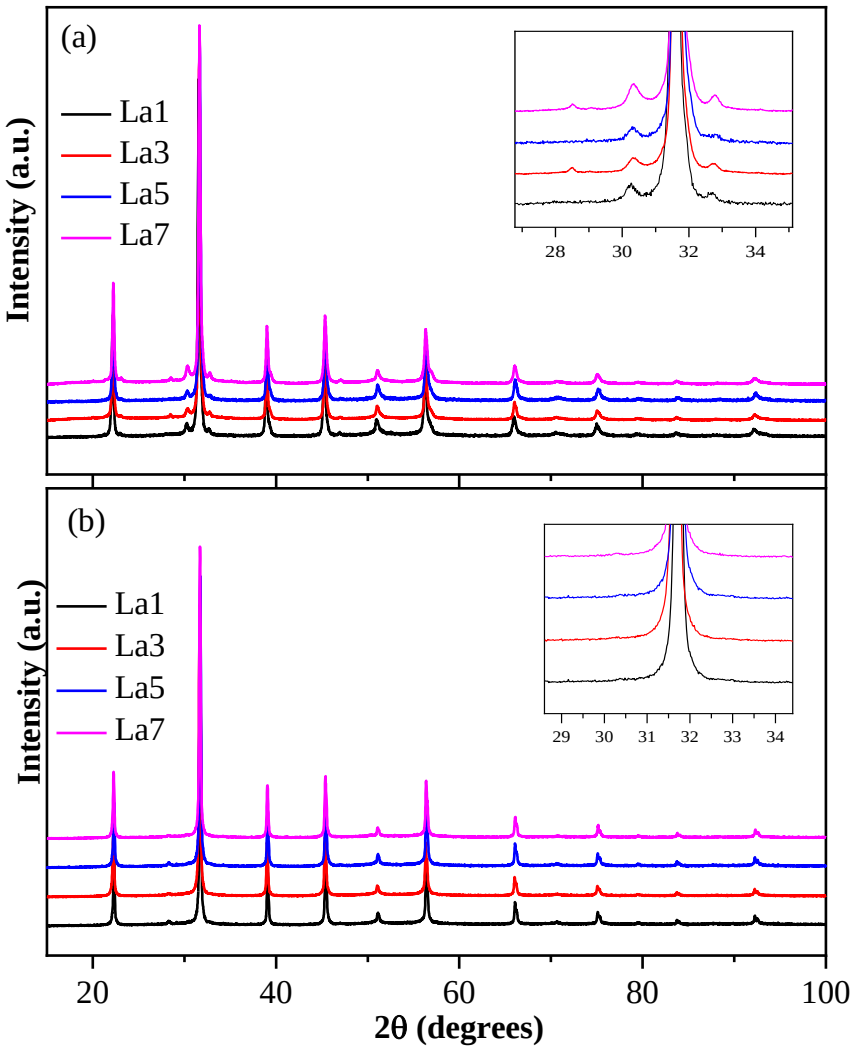

Figure 4.1 XRD patterns of $0.67(Bi_{1-x}La_xFe_{0.97}Ga_{0.03}O_3)$-$0.33(BaTiO_3)$ where x=0.01 (La1), 0.03 (La3), 0.05 (La5), and 0.07 (La7) (a) calcined at 850 ℃ and (b) sintered at 980 ℃ for 2 hours and annealed at 550 ℃ for 12 hours.

The obtained refined XRD patterns fit exhibit excellent agreement between the observed and calculated patterns, as evidenced by the low values of the reliability factor of the weighted pattern (R_{wp}) ranging from 8.57 % to 11.8 % (less than 15%), the reliability factor of patterns (R_p) ranging from 6.53% to 8.99% (less than 15%), and the goodness of fit indicator (χ^2) ranging from 1.49 to 1.89 (less than 2).

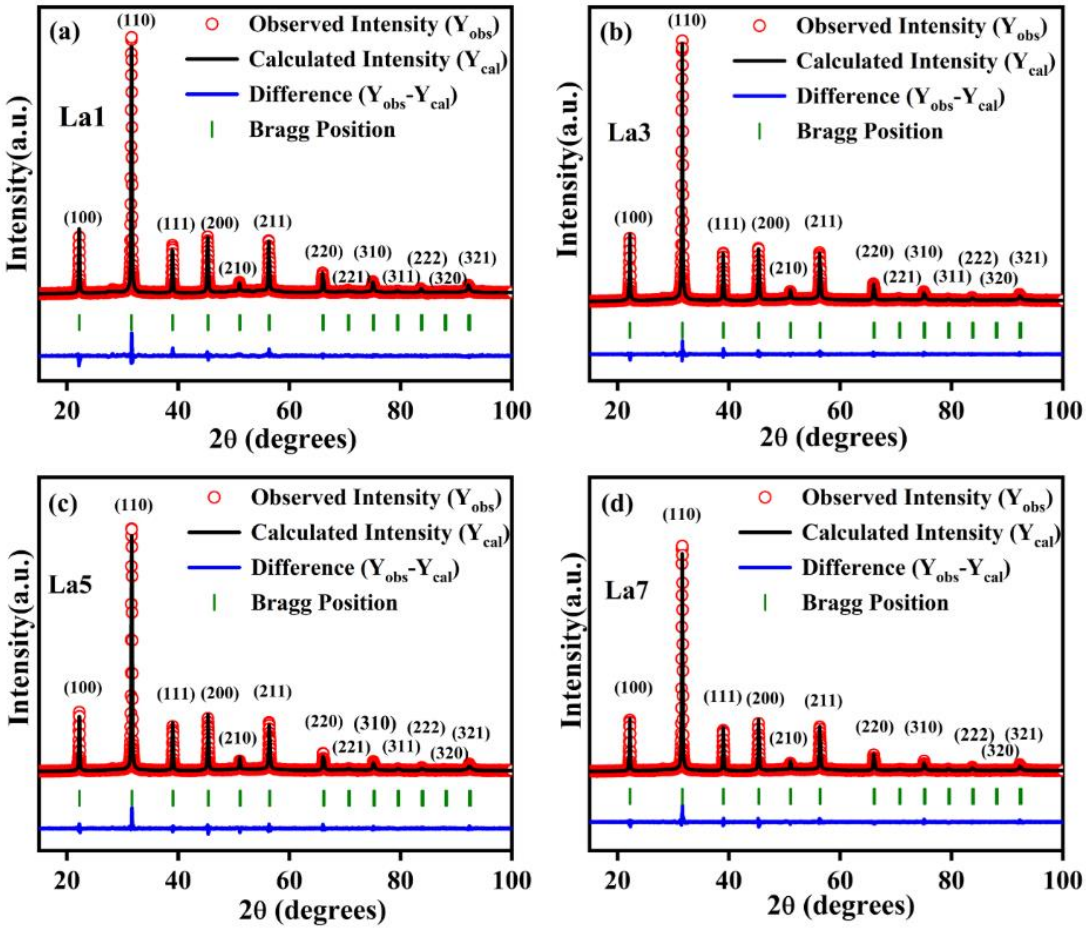

Figure 4.2 The Rietveld refined XRD patterns fit using cubic $Pm\bar{3}m$ space group for $0.67(Bi_{1-x}La_xFe_{0.97}Ga_{0.03}O_3)$-$0.33(BaTiO_3)$ where x=0.01(La1), x=0.03(La3), x=0.05(La5), and x=0.07(La7) sintered at 980 ºC for 2 hours and annealed at 550 ºC for 12 hours.

All the diffraction peaks of different compositions were indexed and refined to the $Pm\bar{3}m$ space group confirming the single pseudocubic phase formation with lattice parameters of 4.0005(1) Å for La1, 3.9988(6) Å for La3, 3.9954(2) Å for La5 and 3.9975(1) Å for La7. Additionally, the peak positions in the XRD patterns remain nearly unchanged, and there is only a slight variation in the lattice parameters as the La concentration increases. This can be attributed to isovalent substitution and the comparable ionic radii between

the A-site, Bi^{+3} (~1.03 Å) and La^{+3} (~1.032 Å) and B-site Fe^{+3} (~0.645Å) and Ga^{+3} (~0.62 Å) cations [188].

Table 4.1. Lattice parameters and refinement factors of $0.67(Bi_{1-x}La_xFe_{0.97}Ga_{0.03}O_3)$-$0.33(BaTiO_3$ where x=0.01(La1), x=0.03(La3), x=0.05(La5), and x=0.07(La7) sintered at 980 ^{0}C for 2 hours and annealed at 550 ^{0}C for 12 hours.

Composition	**Space group**	**Lattice parameter (a=b=c) (Å)**	**Cell Volume (Å^3)**	**R_p**	**R_{wp}**	**χ^2**
La1	$Pm\bar{3}m$	4.0005(1)	64.02(4)	8.99	11.8	1.89
La3	$Pm\bar{3}m$	3.9988(6)	63.94(5)	6.53	8.57	1.49
La5	$Pm\bar{3}m$	3.9954(2)	63.78(1)	7.88	10.2	1.80
La7	$Pm\bar{3}m$	3.9975(1)	63.88(1)	7.45	9.60	1.58

The comparable sizes of these ions facilitate their substitution within the crystal lattice without causing significant lattice distortion. Commonly, it has been reported in previous studies that La doping can enhance the centro-symmetry in the crystal structure [222].

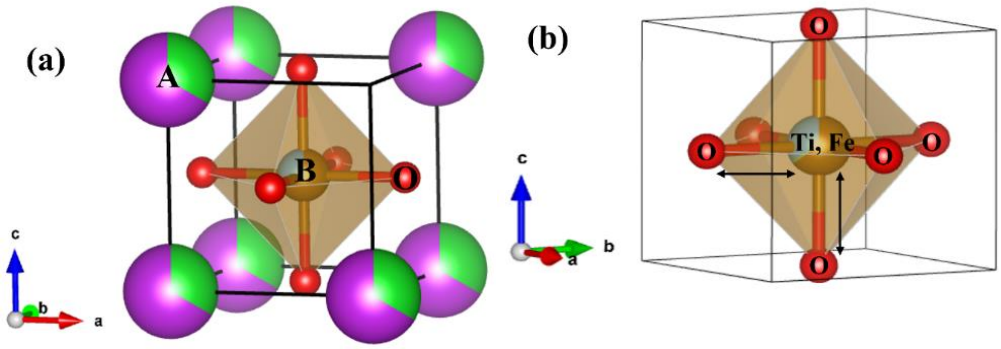

Figure 4.3 Schematic ball and stick diagram of (a) perovskite unit cell (b) Fe/Ti-O_6 octahedra in $0.67(Bi_{0.99}La_{0.01}Fe_{0.97}Ga_{0.03}O_3)$-$0.33(BaTiO_3)$ piezoceramics.

Figure 4.3 (a) illustrates the ball and stick model for the perovskite unit cell and Figure 4.5 (b) depicts the Fe/TiO_6 octahedra used to calculate bond length (Fe/Ti-O) bond length. The calculated Fe/Ti-O bond length for x =0.01, 0.03, 0.05 and 0.07 are 1.8989 Å, 1.8921 Å, 1.8948 Å, and 1.9000 Å, respectively.

4.3.1.2 FTIR Analysis

Figure 4.4 illustrates the room temperature FTIR spectra of all the samples measured in KBr mode. The presence of a sharp band in the range of 500-600 cm^{-1} confirms the formation of the perovskite phase, corresponding to the characteristic "TiO_6/FeO_6" octahedral vibrations [224]. These absorptive bands can be attributed to the bending and stretching vibrations of Fe/Ti-O bonds within the Fe/Ti-O_6 octahedra present in the perovskite structure [193]. The broad absorptive band observed in the range of 3000-3600 cm^{-1} corresponds to the antisymmetric and symmetric stretching vibrations of the O-H groups, while the band around 1700 cm^{-1} arises from the bending vibration of the H-O-H bonds [189]. The presence of these bands can be attributed to the hygroscopic nature of KBr, leading to the adsorption of molecular water [225]. The observed wavenumbers corresponding to absorption bands for x=0.01, 0.03, 0.05 and 0.07 are 592.782 cm^{-1}, 595.957 cm^{-1}, 594.72 cm^{-1} and 592.248 cm^{-1} respectively.

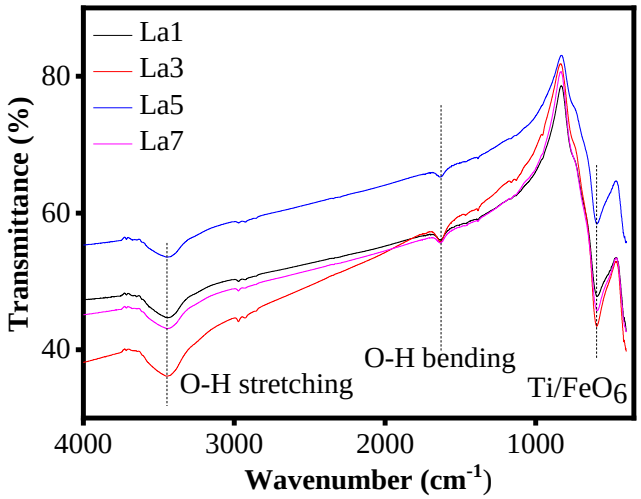

Figure 4.4 FTIR spectra of $0.67(Bi_{1-x}La_xFe_{0.97}Ga_{0.03}O_3)$-$0.33(BaTiO_3)$ where x=0.01(La1), x=0.03(La3), x=0.05(La5), and x=0.07(La7).

The Fe/Ti-O bond length can be calculated using the relation $k = 17/r^3$, , where k is force constant and r is bond length. Force constant can be calculated using the relation $f = \sqrt{k/\mu}/2\pi$, where f is frequency of vibration and μ is effective mass. For x values of 0.01, 0.03, 0.05, and 0.07, the calculated values of Ti/Fe-O bond lengths were determined to be 1.8760 Å, 1.8693 Å, 1.8719 Å, and 1.8771 Å, respectively. Similarly, the calculated values of Ti/Fe-O bond lengths for the corresponding x values from Rietveld structure refinement with XRD pattern were found to be 1.8989 Å, 1.8921 Å, 1.8948 Å, and 1.9000 Å, respectively. This confirms the close agreement in the calculated bond lengths from XRD and FTIR with the standard Fe-O and Ti-O bond lengths.

4.3.1.3 X-ray Photoelectron Spectroscopy Analysis

The presence of multiple ions and the volatile nature of Bi in the $0.67(Bi_{1-x}La_xFe_{0.97}Ga_{0.03}O_3)$-$0.33(BaTiO_3)$ system can lead to charge imbalance and the formation of oxygen vacancies. This highlights the importance of investigating the oxidation state to understand and correlate with other functional properties, as defects that can influence

different relaxation mechanisms. The complete XPS spectra of $0.67(Bi_{1-x}La_xFe_{0.97}Ga_{0.03}O_3)$-$0.33(BaTiO_3)$ pellets for x=0.01(La1) and x=0.03(La3) are depicted in Figure 4.5 (a-b). Using standard calibration, the XPS binding energy scale was charge corrected using reference C-1s peak fixed at 284.8 eV using CASA XPS software. Additionally, no extra undesired peaks of any other elements or impurities were observed confirming the high purity of samples. The magnified XPS spectrum in the range 525 – 535 eV for O1s is presented in Figure 4.6. The O-1s spectrum were fitted using Asymmetric Lorentzian (LA) function superimposed on Shirley background. LA function is Voigt-like function, a convolution of a generalized Lorentzian function with a Gaussian function. It takes into accounts both peak asymmetry and Gaussian character for obtaining good XPS fitting. The asymmetric peak was de-convoluted to two components with one peak positioned at binding energy of approximately 529 eV and other at binding energy of approximately 531 eV. The peak observed at lower binding energy (LBE) represented by OI corresponds to lattice oxygen ions bound to Ti-2p/Fe-2p in BFO-BTO lattice while the peak observed at high binding energy (HBE) represented by OII are attributed to O^{2-} /O^- ions induced by oxygen vacancies ($V_O^{\bullet\bullet}$), or the loss of oxygen [226]. However, it is generally accepted that the creation of PNR and, subsequently, the relaxor behavior and diffuse transitions are caused by both La^{3+} and/or oxygen vacancies, which disrupts the translational symmetry of the lattice [181], [227], [228], [229]. The ratio of the area under curve of the two components of O-1s peaks (OI/OII) for each composition, revealing values of 61.30/38.78 for La1, 78.80/21.20 for La3, 74.36/25.64 for La5 and 77.20/22.80 for La7. This analysis provides insights into the concentration of oxygen vacancies ($V_O^{\bullet\bullet}$), and their influence on the system. The XPS spectra of Fe-2p lines were also examined to study the Fe valence state. The XPS spectra of Fe-2p lines are shown in Figure 4.7. By asymmetric Lorentzian curve fitting the low binding energy peak

corresponding to $2p_{3/2}$ was further resolved into two peaks, one peak around 709 eV and other around 711 eV.

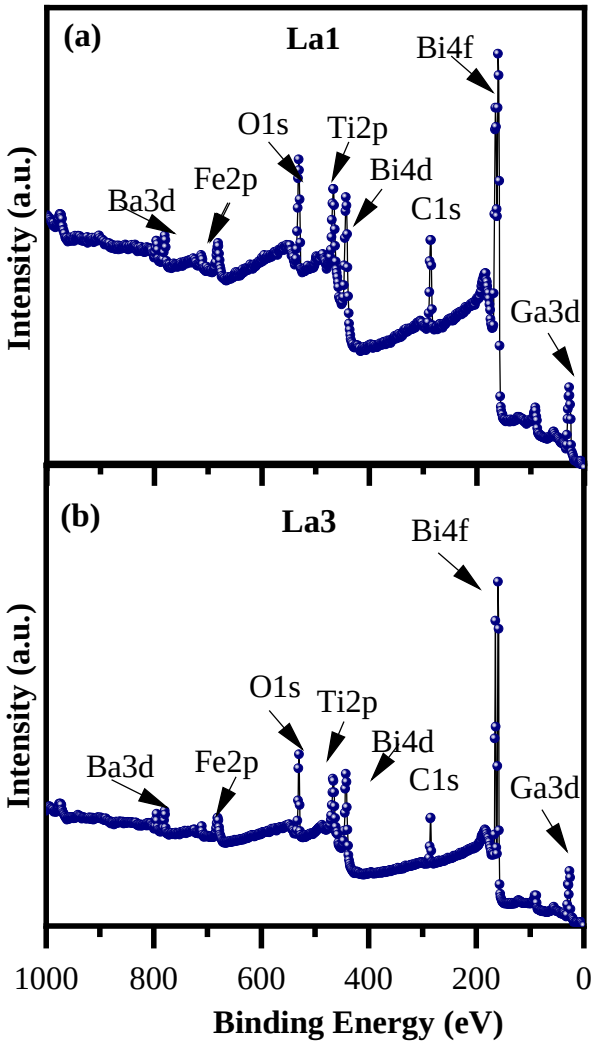

Figure 4.5 Complete XPS spectra of (a) x=0.01(La1), and (b) x=0.03(La3) for $0.67(Bi_{1.05-x}La_xFe_{0.97}Ga_{0.03}O_3)$-$0.33(BaTiO_3)$ ceramics.

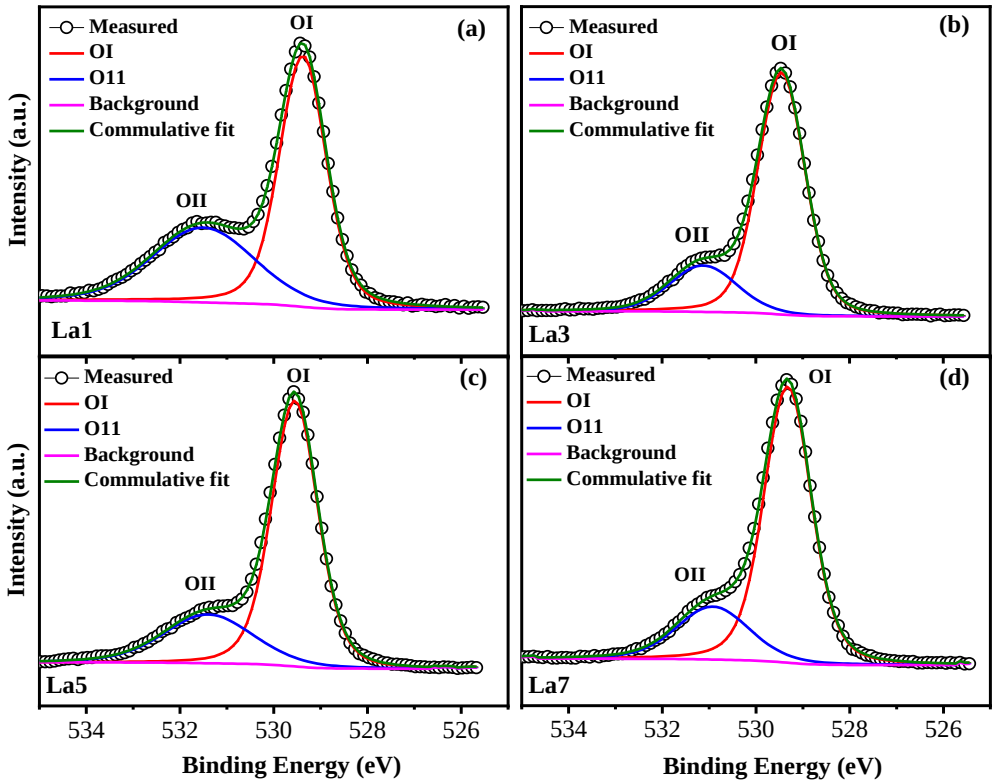

Figure 4.6 XPS spectra of O1s state for $0.67(Bi_{1-x}La_xFe_{0.97}Ga_{0.03}O_3)$-$0.33(BaTiO_3)$ ceramics (a) x=0.01(La1), (b) x=0.03(La3), (c) x=0.05(La5), and (d) x=0.07(La7).

The peak at 709 eV is attributed to the Fe^{2+} valence and the one around 711 eV is representing Fe^{3+} as the lower binding energy peak refers to low valence state. The reduction of the Fe^{3+} to Fe^{2+} follows the creation of oxygen vacancies to maintain the charge neutrality. In accordance with the defect theory, the charge defect dipoles are formed between oxygen vacancies and Fe^{+2} which creates the internal bias field and hinders the domain wall motion due to which the dielectric and piezoelectric properties deteriorate [184]. The estimated ratio of the area under the Fe 2p component peak (Fe^{3+}/Fe^{2+}) are 63:37 for La1, 67:33 for La3, 56:44 for La5 and 62:38 for La7 indicating dominance of Fe^{3+} valence state throughout the samples. The XPS binding energy peak positioned respectively at ~711 eV and ~724 eV are the spin orbit doublets $2p_{3/2}$ and $2p_{1/2}$ corresponding to Fe^{3+}.

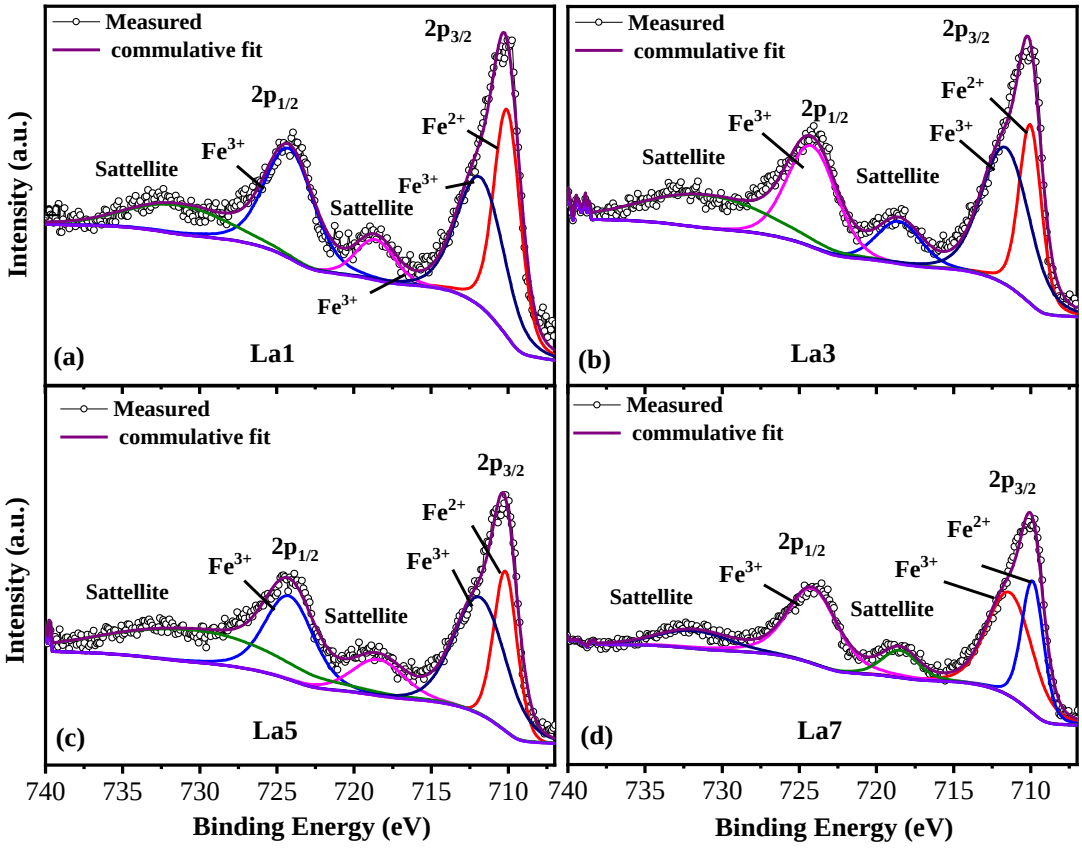

Figure 4.7 XPS spectra of Fe2p state for $0.67(Bi_{1-x}La_xFe_{0.97}Ga_{0.03}O_3)$-$0.33(BaTiO_3)$ ceramics (a) x=0.01(La1), (b) x=0.03(La3), (c) x=0.05(La5), and (d) x=0.07(La7).

Furthermore, the satellite peaks around ~718 and ~731 were observed as a result of shake up process where the photoelectron ejection from 2p shell leads to loss of kinetic energy which is consumed in transition from 3d to empty 4s orbital. The high sintering temperature can cause the formation of defects such as oxygen vacancies or charge defects due to variable valance in the material. These defects can act as electron traps, leading to an increase in the leakage current. The oxygen vacancies can reduce Fe^{3+} ions to Fe^{2+} ions, leading to a decrease in the number of Fe^{3+} ions available for charge compensation. The ratio of OI/OII and Fe^{3+}/Fe^{2+} is maximum for x=0.03 indicating minimum oxygen vacancy formation and highest Fe^{+3} contribution. Figure 4.8 depicts the XPS spectra of Bi-4f state. The peak at high binding energy of around ~164 eV represents

Bi $4f_{5/2}$ and other peak around ~158 eV corresponds to Bi $4f_{7/2}$ which are separated by ~5.3 eV indicating the presence of Bi in +3 valence[230]. Additionally, the presence of La^{3+} ions in the system can also lead to the formation of additional defects, such as La-O anti-site defects, which can also contribute to the large leakage current. Increasing the concentration of La ions from x=0.01 to 0.07 can affect the properties of the material. Changing the doping concentration can lead to an enhancement of the ferroelectric properties and increase in dielectric constant, but also it can reduce the thermal stability of the material.

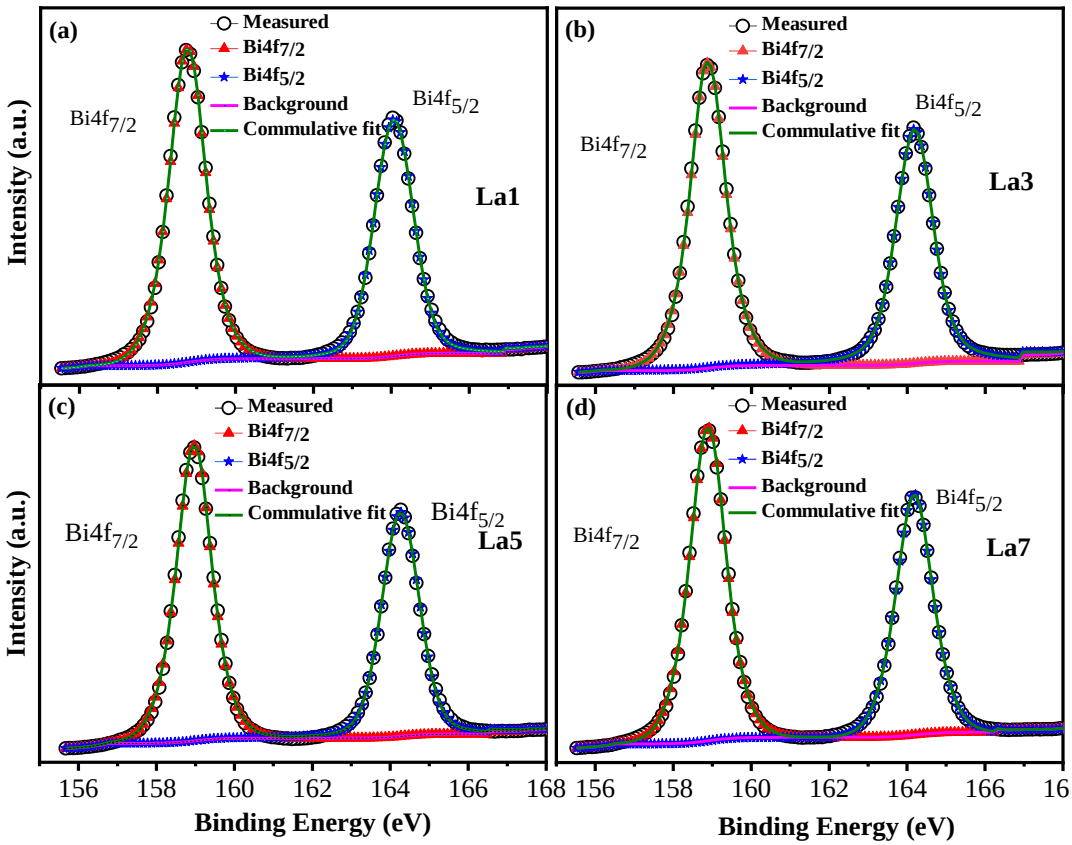

Figure 4.8 XPS spectra of Bi4f state for $0.67(Bi_{1-x}La_xFe_{0.97}Ga_{0.03}O_3)$-$0.33(BaTiO_3)$ ceramics (a) x=0.01(La1), (b) x=0.03(La3), (c) x=0.05(La5), and (d) x=0.07(La7).

4.3.2 Microstructural Studies

Figure 4.9 (a-d) presents representative fractured SEM micrographs of the sintered pellets of $0.67(Bi_{1-x}La_xFe_{0.97}Ga_{0.03}O_3)$-$0.33(BaTiO_3)$ ceramics and their grain size distribution for the different compositions. All the samples exhibit a dense microstructure with negligible porosity and high density ranging from 7.35 g/cm^3 to 7.59 g/cm^3, indicating optimized sintering conditions and a relative density greater than 97 %. Since the grain size is strongly influenced by the sintering technique, temperature and dwelling time, the fine grain size may be one of a consequence of short dwelling time and air quenching. The densely packed clear grain size distribution can be observed in all the samples. Sequential observations reveal a similar pattern of domain states, grain size distribution, based on the analysis of more than 100 grains, is provided in the Figure 4.9 (e-h). characterized by micron-sized domains, twin polar tweed-like structures, and polar nanodomains or clusters in all the samples. The statistical representation histogram of the histogram histogram of the grain size distribution, based on the analysis of more than 100 grains, is provided in the Figure 4.9 (e-h). Although the average grain size slightly increases with increasing doping concentrations, it remains below 1.5 μm, which can be attributed to the low diffusivity of rare earth ions [188].

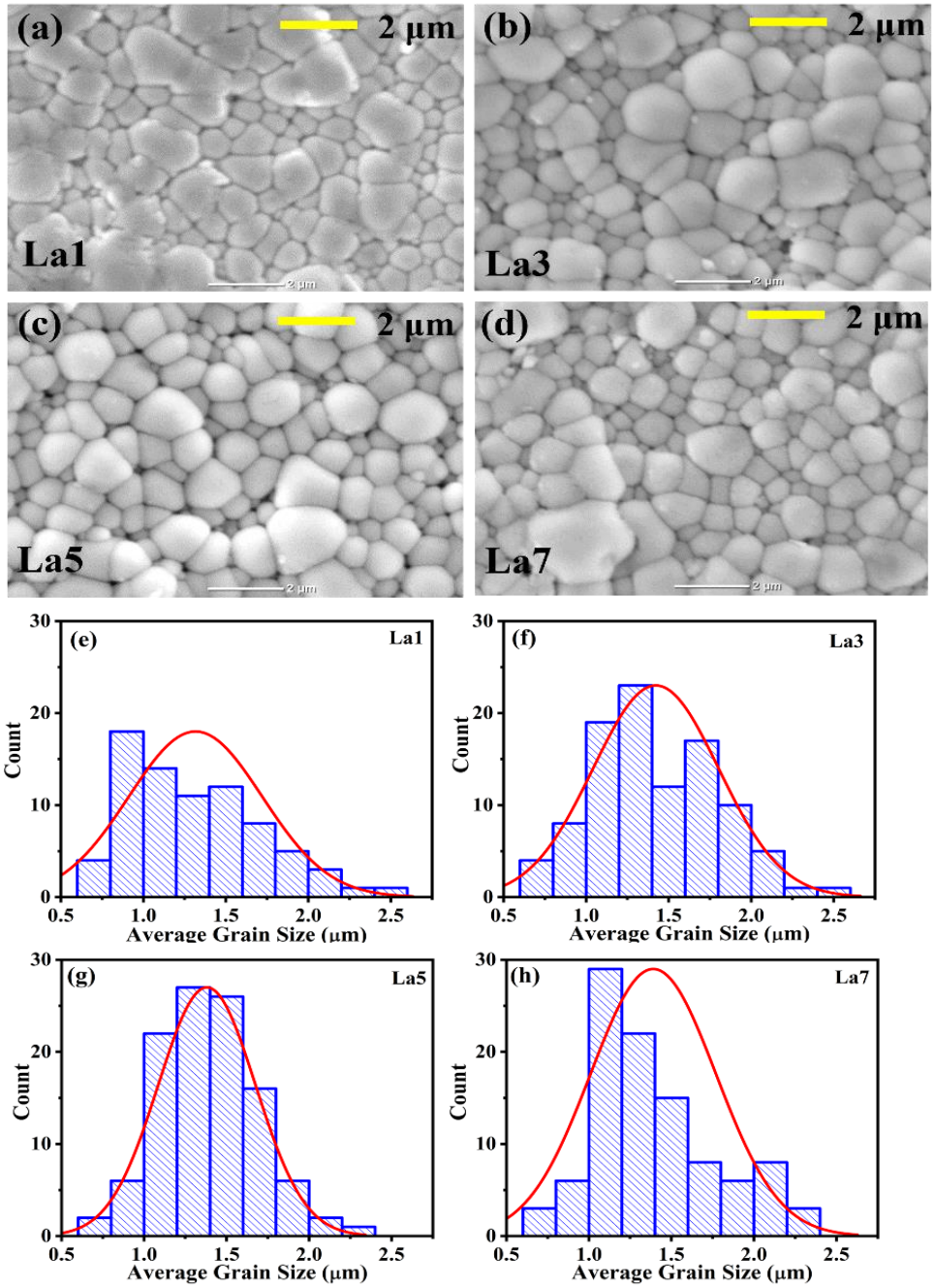

Figure 4.9 SEM images and grain size distribution for (a, e) x=0.01(La1), (b, f) x=0.03(La3), (c, g) x=0.05(La5), (d, h) x=0.07(La7) and for $0.67(Bi_{1-x}La_xFe_{0.97}Ga_{0.03}O_3)$-$0.33(BaTiO_3)$ samples.

4.3.3 Dielectric and Ferroelectric Studies

The temperature-dependent dielectric permittivity and dielectric loss (tanδ) as a function of frequency, ranging from 1.26 kHz to 160 kHz, are depicted in Figure 4.10 (a-

d) for the $0.67(Bi_{1-x}La_xFe_{0.97}Ga_{0.03}O_3)$-$0.33(BaTiO_3)$ where $x \leq 0.07$. A comparison of the dielectric permittivity values in the temperature range of 300-400 ^{0}C and frequency dependent dielectric permittivity plots for different compositions are illustrated in Figure 4.10 (e) and Figure 4.10 (f), respectively. The observed dielectric anomalies are diffused and show the strong frequency dispersion and with increasing frequency the peak corresponding to maximum dielectric constant shifts to higher temperatures for all the compositions indicating relaxor like behavior. Previously it is widely acknowledged that the introduction of La^{3+} ions disrupt the translational symmetry of the lattice, leading to a form of disorder that fosters the formation of polar nanodomains and, consequently, imparts relaxor characteristics [181], [210], [227], [228]. With increasing concentration of La^{+3} from x=0.01 to 0.07, there is a significant enhancement in both the room temperature value as well as maximum value of the dielectric permittivity. At room temperature, the dielectric permittivity increases from 803 to 1393 and the maximum dielectric permittivity value, at peak temperature, increases from 4100 to 24066 at 10 kHz frequency, reflecting a multifold improvement in dielectric response. High values of dielectric permittivity at low frequencies shown in Figure 4.10 (a-d) could be attributed to Maxwell-Wagner type contribution. Space charge polarization related to oxygen vacancies contribute to the dielectric response at lower frequencies. As the frequency increases the value of dielectric permittivity decreases as a result of inability of dipoles to reorient themselves with the applied electric field at higher frequencies. At higher frequencies, the internal hindrance becomes more significant, leading to the dissipation of energy as heat. This dissipation reduces the ability of the material to store electric charges and hence decreases the dielectric permittivity. These observations highlight the temperature and compositional dependence of the dielectric properties and suggest the influence of charge defects and oxygen vacancies on the dielectric response. The

anomalies observed around 300 ℃ in the dielectric loss tangent can be attributed to transient reactions involving oxygen vacancies and different redox reactions of Fe valence, or to transitions in electrical ordering [231]. These are not intrinsic but due to presence of charge defects. The room temperature dielectric loss values at 10 kHz for x=0.01, 0.03, 0.05 and 0.07, are 0.13947, 0.12103, 0.25668, and 0.57611, respectively. As the temperature increases, the dielectric loss increases significantly due to thermally activated processes, leading to an enhanced contribution of space charge polarization associated with oxygen vacancies [231].

The diffuse nature observed in the dielectric response of relaxor ferroelectrics is attributed to the existence of polar nanoregions (PNRs) within the material. The coexistence of smaller grains embedded at the grain boundaries of larger grains may forms clusters known as Polar Nanoregions (PNR). PNRs represent small regions where the local electric dipoles exhibit fluctuations or reorientations. These PNRs disrupt long-range ordering and the reduced grain size, shifts the temperature of the peak dielectric permittivity (T_m) to higher temperatures, indicating diffused phase transitions. This phenomenon can be explained by the modification of domain patterns analogues to martensitic transformation theories, where the lowering of elastic energy due to isovalent-ion replacement or grain size reduction induces relaxor features [181]. The extent of diffuseness in the dielectric response serves as an indicator of the distribution of relaxation times linked to polar nanoregions (PNRs) of various sizes and orientations. These PNRs play a significant role in shaping the distinctive characteristics of relaxor ferroelectrics and are fundamental for comprehending their behavior. The presence of diffuseness is intimately associated with the lack of a distinct Curie temperature, which is commonly observed in traditional ferroelectric materials. Complex perovskite ferroelectric systems often exhibit frequency-dependent diffuse phase transitions,

deviating notably from the Curie-Weiss law, especially when multiple ion occupations occur at the A/B-sites of the ABO_3 perovskite.

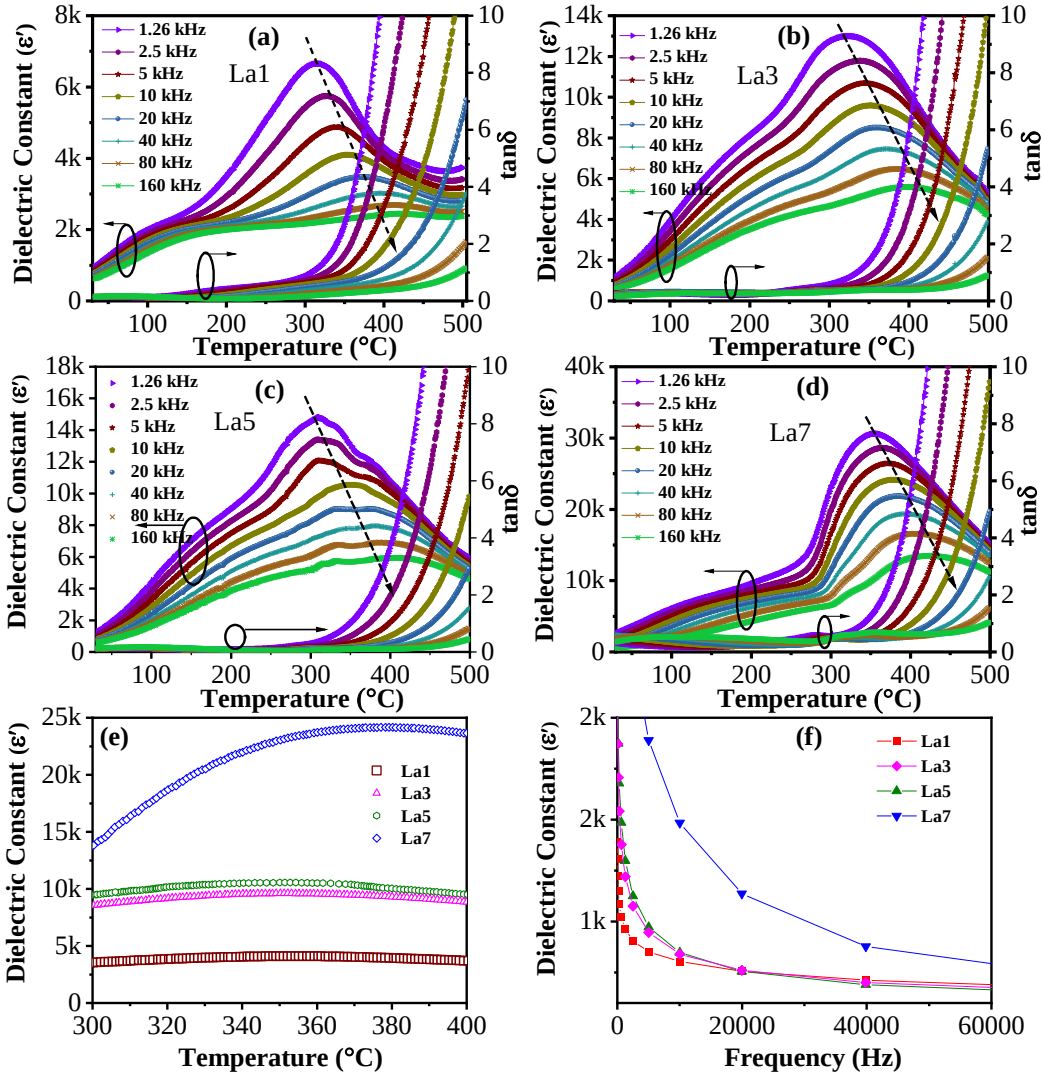

Figure 4.10 Temperature dependent dielectric permittivity and dielectric loss plots as a function of frequency in the range 1.26 kHz to 160 kHz for x=0.01(La1), (b) x=0.03(La3), (c) x=0.05(La5), (d) x=0.07(La7) (e) comparison of dielectric constant at 10 kHz and (f) frequency dependent dielectric constant for all compositions.

Compositional fluctuations in perovskite ferroelectrics can generally give rise to diffuse phase transitions. The diffuseness of the phase transition can be quantified by using the semi-empirical expression proposed by K. Uchino and Nomura also known as modified Curie-Weiss law:

$$\frac{1}{\varepsilon_r} - \frac{1}{\varepsilon_m} = C^{-1}(T - T_m)^{\gamma} \qquad [T > T_m] \qquad (4.1)$$

Where ε_m is maximum dielectric constant value at T_m, C is Curie like constant and γ is an exponent varying in the range $1 < \gamma < 2$ where $\gamma \sim 1$ when the transition shows Curie Weiss behavior for normal ferroelectric and $\gamma \sim 2$ for diffused phase transitions/relaxors. The γ exponent is also known as degree of diffuseness [67], [232]. The more the normal ferroelectric character, the smaller the γ values are. Figure 4.11 displays the combined logarithmic plots of the $\ln(1/\varepsilon_r - 1/\varepsilon_m)$ vs. $\ln(T-T_m)$ along with the corresponding γ values for all the compositions at 10 kHz.

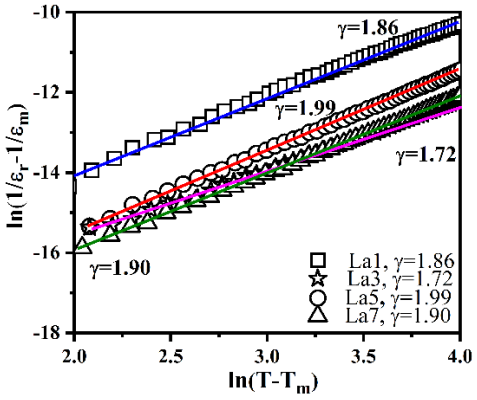

Figure 4.11 Modified Curie-Weiss law plots for characterization of diffuseness parameter γ at 10 kHz for $0.67(Bi_{1-x}La_xFe_{0.97}Ga_{0.03}O_3)$-$0.33(BaTiO_3)$ where x=0.01(La1), x=0.03(La3), x=0.05(La5), and x=0.07(La7).

As shown in Figure 4.11, a good linear fit was obtained whose slope determines the γ value. It can be observed that all the γ values are close to 2 which signifies the relaxor behavior. The fine grain size, and the weakening of long-range ordering due to substitution, enhances the relaxor behavior [233].

Furthermore, to gain a deeper understanding of the relaxor ferroelectric behavior and the evolution of dielectric relaxation, the Vogel-Fulcher (VF) model fitting was employed as shown in Figure 4.12. The permittivity maxima temperature (T_m), at which dielectric permittivity is maximum, is found to obey Vogel-Fulcher equation [215], [234],

[235]. The dipoles interactions are also taken into account in this particular model and at some particular temperature known as freezing temperature (T_{VF}) the dipoles are frozen. The relation can be expressed as follows:

$$f = f_0 e((T_0)/(T_m\text{-}T_{VF})) \qquad (4.2)$$

Where ƒ is measurement frequency, f_0 is attempt frequency of dipole reorientation or pre-exponential factor, T_o denotes the ratio of Activation Energy (E_a) and Boltzmann constant (k_B) and T_{VF} is called freezing temperature, below which the dynamic reorientation of the dipolar cluster polarization is not thermally activated (relaxing dipoles freeze and become static). The well fitted curves for Vogel-Fulcher model accounts for the upward increasing trend in freezing temperature from ~465 K for x=0.01 to ~551 K for x=0.07 composition while the trend is opposite for activation energy dropping from ~0.61 eV to 0.07 eV as the composition increases. This means the barrier between the potential wells is decreasing leading to increased dielectric loss [236]. The weaker interaction between the polar nanoregions (PNRs) due to higher activation energy makes it more challenging to establish a long-range ordered dipole configuration in an electric field. The increased dielectric permittivity at lower frequencies in La7 can be due to the combined contributions from various polarization mechanisms. The lower relaxation times and lower activation energies in these samples facilitate the dynamic reorientation of dipoles in the presence of an electric field.

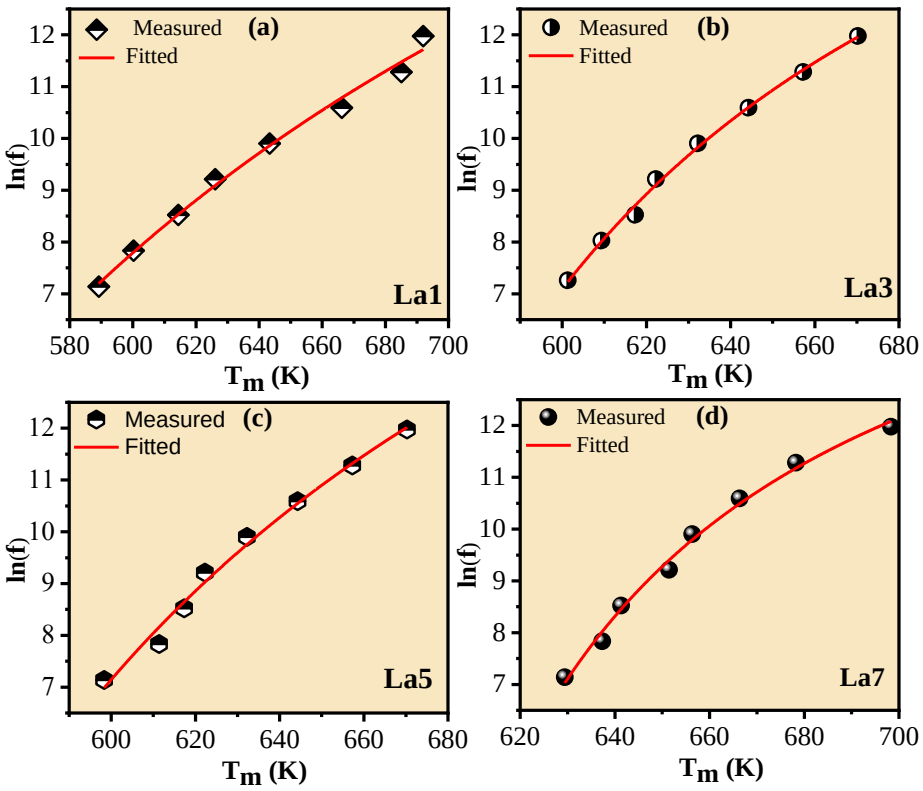

Figure 4.12. Vogel Fulcher curve fitting for $0.67(Bi_{1-x}La_xFe_{0.97}Ga_{0.03}O_3)$-$0.33(BaTiO_3)$ with compositions (a) x=0.01(La1), (b) x=0.03(La3), (c) x=0.05(La5), and (d) x=0.07(La7).

According to previous research reports on the undoped BF-BT, ternary BF-BT ceramics and La-doped $0.56BiFeO_3$-$0.44BaTiO_3$, the poor insulation and high dielectric loss resulted in rounded ferroelectric hysteresis loop [84], [100], [102], [185], [196], [237]. However, in the case of 0.67BF-0.33BT, better saturated loops have been observed [102]. The ferroelectric polarization and current hysteresis loops for all the compositions recorded at different applied fields are depicted in Figure 4.13 (a-d). The slim P-E loops were observed in all the samples. It can be observed that as the concentration of La^{3+} increases from x=0.01 to 0.07, the overall remnant polarization value decreases from ~8.407 to 3.946 $\mu C/cm^2$. The appearance of both the relaxor-ferroelectric phase and pseudocubic phase with increasing doping concentration may lead to a progressive

decrease in the Pr values. Similar observations have been noted in previous research on ceramics derived from BF-BT compositions [238]. The maximum P_r value of 12.284 $\mu C/cm^2$ and a minimum coercive field (E_c) of ~30.9489 kV/cm is obtained for x=0.03 composition.

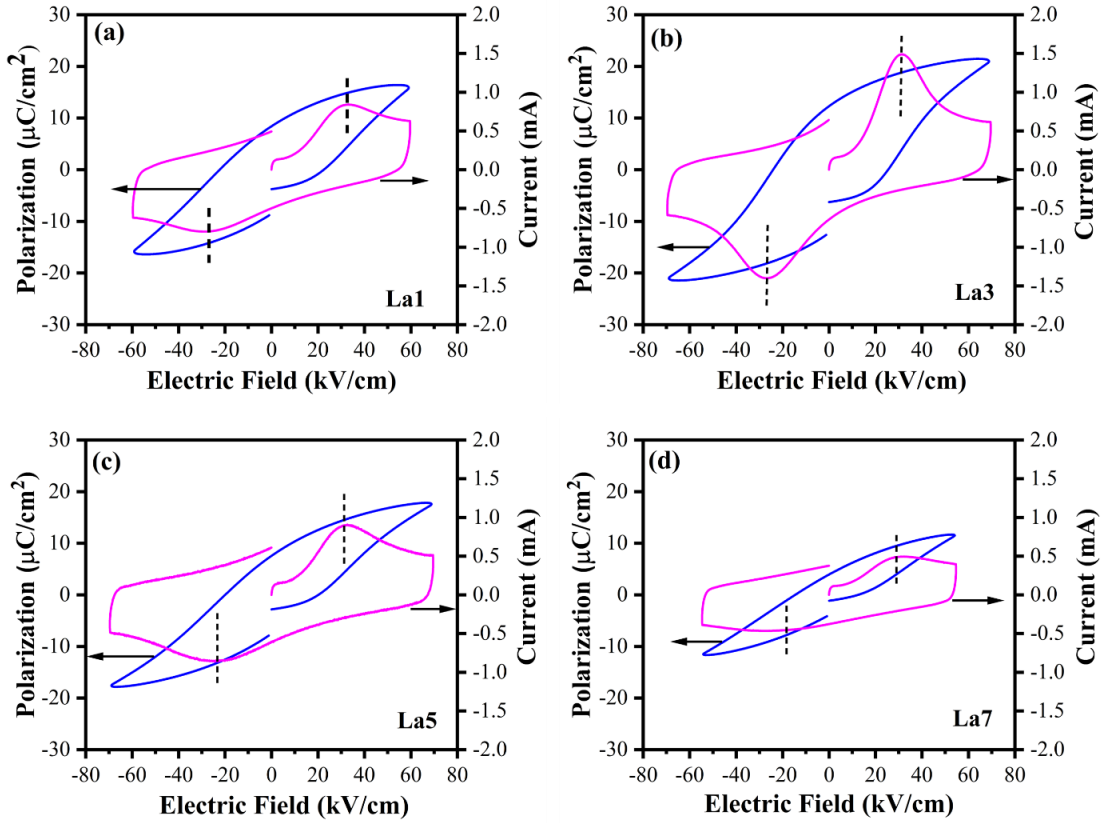

Figure 4.13 Polarization vs Electric field and Current response hysteresis loops for $0.67(Bi_{1-x}La_xFe_{0.97}Ga_{0.03}O_3)$-$0.33(BaTiO_3)$ where (a) x=0.01(La1), (b) x=0.03(La3), (c) x=0.05(La5), (d) x=0.07(La7).

The value of coercive field for x=0.01, 0.03, 0.05 and 0.07 is 32.490 kV/cm, 30.949 kV/cm, 32.630 kV/cm and 31.093 kV/cm, respectively. The emergence of random field close to dipolar defects may provide an explanation for the reduced coercive field. The activation barrier necessary for the nucleation of domains can be considerably lowered by the random field around dipolar defects, resulting in a lower coercive field [186], [239]. The well-defined switching peaks in the current response curves confirms the ferroelectric nature and the saturation of P-E loops. Figure 4.14 (a) illustrates the leakage

current plots for all the compositions. The results of leakage current measurement reveal the resistivity values of the order of 10^8 (ohm.cm) even at an applied field of 30 kV/cm signifying the minimization of losses and defects in the prepared samples. The current density (A/cm^2) as a function of La doping concentration, measured at an applied field of 1 kV/cm, 10 kV/cm, 20 kV/cm and 30 kV/cm are of the order of 10^{-7},10^{-6}, 10^{-5} and 10^{-5}, respectively. It is evident that the enhanced resistivity and the current density values were obtained at the higher applied electric fields also.

To further investigate the ferroelectric switching behavior and to differentiate the switchable and non-switchable polarization contribution in the prepared compositions, the Positive Up Negative Down (PUND) measurements were carried out for all the samples as shown in Figure 4.14 (b). The first pulse functions as the pre-write pulse. Subsequently, the initial read pulse is positively switched, followed by an unswitched pulse, a negatively switched pulse, and finally, a negatively unswitched pulse. In this experimental setup, a series of five pulses is employed. Initially, Pulse 0 polarizes the sample, establishing a specific polarization state. Subsequently, Pulse 1 initiates a reversal of the polarization. Pulse 2, aligned with Pulse 1, is designed not to induce switching. Pulses 3 and 4 replicate the actions of Pulses 1 and 2 but in the opposite direction. The switching phase denoted by 1 is evident in Figure 4.10 (b) for La1, La3, La5 and La7 as the applied field increases. Following this, we can observe the maximum polarization was obtained for La3 and the minimum was for La7. If polarization is stable, Pulse 2, applied after a delay, should not induce switching. For La7, the contribution from switchable polarization is maximum indicating the contribution of artifacts.

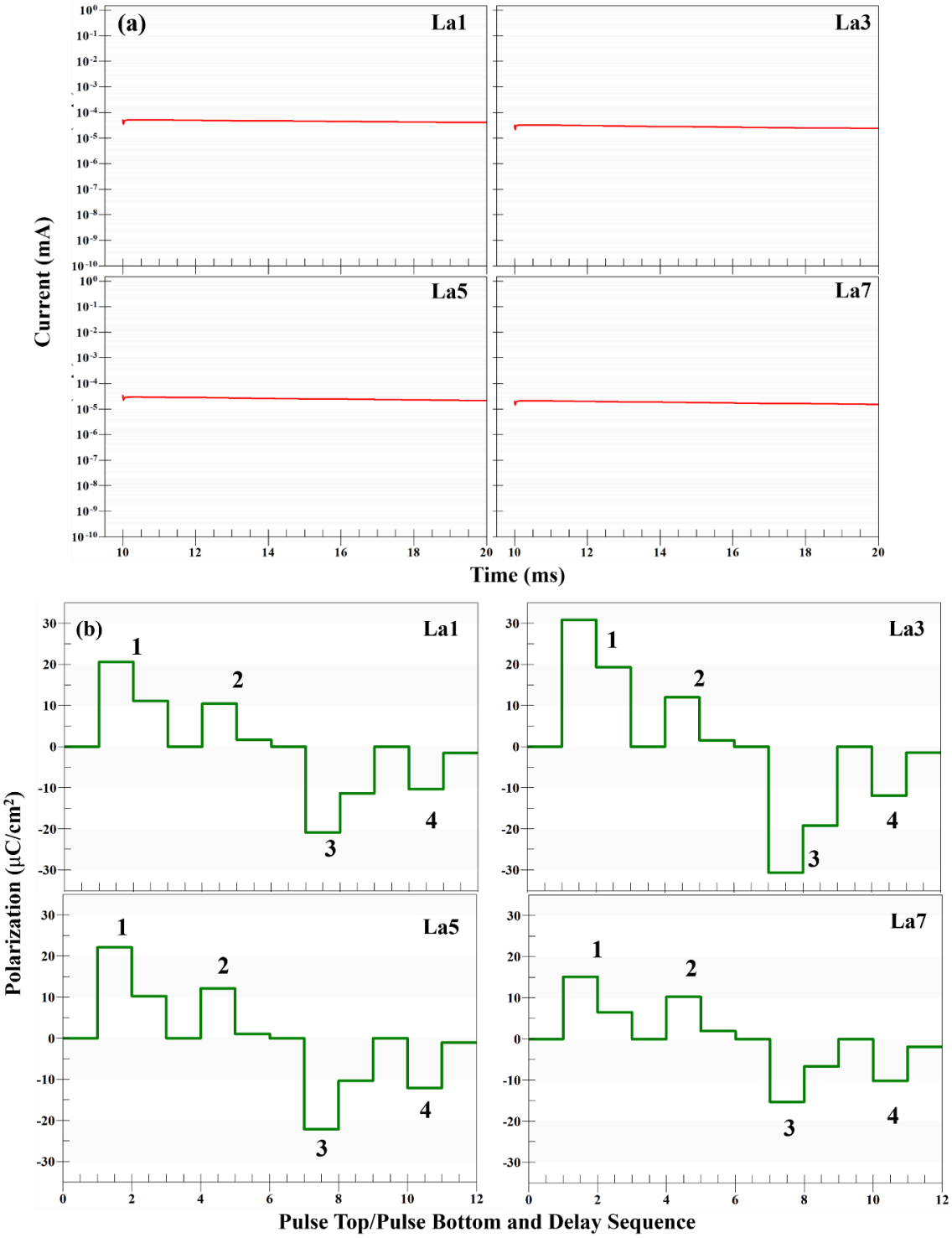

Figure 4.14 (a) Leakage current plot for all compositions performed at an applied field of 30 kV/cm (b)PUND polarization profile for $0.67(Bi_{1-x}La_xFe_{0.97}Ga_{0.03}O_3)$-$0.33(BaTiO_3)$ samples.

4.4 Conclusions

In conclusion, this chapter is focused on the synthesis and characterization of high-temperature lead-free La and Ga modified $BiFeO_3$-$BaTiO_3$ ceramics. The results revealed important insights into the crystal structure, microstructure, chemical composition, dielectric behavior, and ferroelectric properties of the developed material. The analysis of dielectric constant and loss as a function of temperature and frequency demonstrated significant frequency dispersion, indicating relaxor-like behavior. This behavior is attributed to the introduction of La^{+3} ions, which disrupt the long-range ordering and introduce centrosymmetry in the material. To degree of diffuseness was modelled by modified Curie-Weiss law which demonstrates strong relaxor behavior. Furthermore, the dielectric relaxation behavior was analyzed using the Vogel-Fulcher model, which provided valuable information about the activation energy and freezing temperature. The activation energy decreased from approximately 0.61 eV to 0.07 eV as the concentration of La^{+3} dopant increased. This suggests that the presence of La ions affects the relaxation mechanisms and leads to a decrease in the energy barrier for dipole reorientation. The dielectric constant was significantly enhanced, increasing from 4100 to 24066 when compared at a frequency of 10 kHz, as the concentration of La^{+3} dopant increased from x=0.01 to 0.07. The structural and morphological analysis suggests the pseudocubic phase formation with small grain size. Overall, this work demonstrates the effectiveness of simultaneous site engineering, by incorporating La and Ga ions, to enhance the dielectric and ferroelectric properties of the $BiFeO_3$-$BaTiO_3$-based system.